Bulletin of the Seismological Society of America, Vol. 109, No. 3, pp. 1171–1179, June 2019, doi: 10.1785/0120180325

Short Note

Determining Moho Depth beneath Sedimentary Basins Using Regional *Pn* Multiples

by Chunquan Yu,* Zhongwen Zhan, Egill Hauksson, Elizabeth S. Cochran, and Donald V. Helmberger

Abstract The study of the Moho beneath thick sedimentary basins involving natural earthquakes is challenging, as low-velocity materials often cause strong reverberations that mask Moho signals. Here, we develop a method to determine the depth of the Moho by taking advantage of the presence of the sediments. The method utilizes the first *Pn* crustal multiple from regional earthquakes *PnPn* and its differential travel time with respect to *Pn*. *PnPn* is usually weak in amplitude; thus, it is difficult to identify in regions without a sedimentary cover. However, *PnPn* is significantly amplified in the presence of low-velocity sediments because of an increase in the near-surface *P*-to-*P* reflection coefficient. The arrival time, amplitude, and wave shape of *PnPn*, if normalized by the reference *Pn*, are insensitive to earthquake source parameters, such as focal mechanism and focal depth. We demonstrate the potential of this method using both 1D and 2D waveform simulations. Synthetic waveforms suggest that *PmpPn* and *PnPmp* (one *Pn* leg merges to *PmP* near the source or the receiver) largely contribute to the *PnPn* amplitudes, which depend on the near-surface structure at their free-surface *P*-to-*P* reflection points. We further validate the method with two field examples in the Imperial Valley; one is near the United States–Mexico border, and the other is in Oklahoma in the central United States. Both examples suggest that the method can be used to study the Moho either near the source or the receiver.

Introduction

The Mohorovičić discontinuity (or Moho) represents a transition from felsic or mafic rocks in the crust to ultramafic assemblages in the upper mantle (Brown and Mussett, 1993; Christensen and Mooney, 1995). Understanding the structure and nature of the Moho has important implications for the origin and evolution of the continents, crustal isostasy, and mantle dynamics (Watts, 2001; Eaton, 2006; Anderson, 2007; Yu *et al.*, 2016).

Since its discovery, the Moho has been the target of many seismological investigations (Thybo *et al.*, 2013). Controlled-source seismology has been one of the principal approaches to imaging of the Moho since the mid-twentieth century (Prodehl and Mooney, 2012). Both seismic refraction and reflection studies were conducted worldwide to study the detailed Moho transition and crustal structure. Since the late 1970s, passive-source seismology that used converted seismic phase arrivals and phase multiples, also known as receiver function analysis, has become an important technique in the study of crustal structure (e.g., Bath and Stefánsson, 1966; Jordan and Frazer, 1975; Vinnik, 1977; Langston, 1979). Detailed regional waveform modeling has also been conducted to provide constraints on fine structure of the crust and upper mantle (e.g., Helmberger and Engen, 1980; Nyblade *et al.*, 1996; Langston *et al.*, 2002).

It is not always an easy task to image the Moho explicitly, and a detailed understanding of the crust–mantle boundary can still be elusive (Eaton, 2006). There are several problems that are encountered when using these traditional techniques to image the Moho. For example, the crust–mantle boundary may correspond to a gradual transition from mafic rocks to ultramafic assemblages (O'Reilly and Griffin, 2013). Conventional seismic imaging methods, such as receiver functions, generally do not easily detect weak signals from a crust–mantle boundary that is transitional over a large depth range or with small impedance contrast. One example is the difficulty detecting these signals beneath

*Now at Department of Earth and Space Sciences, Southern University of Science and Technology, 1088 Xueyuan Road, Nanshan District, Shenzhen, Guangdong 518055, China.

the Colorado plateau (Gilbert *et al.*, 2007). It is also questionable whether the seismically defined Moho, either by near-vertical seismic reflection or wide-angle seismic refraction, is indeed coincident with the crust–mantle boundary (Mooney and Brocher, 1987; O'Reilly and Griffin, 2013). Another complication is caused by thick unconsolidated sediments. In conventional *P*-wave receiver functions, multiples from unconsolidated sediments can arrive nearly coincident with the Moho *P*-to-*S* conversion, with the amplitude of the former larger than that of the latter. Although a few advances have been made to mitigate the effect of sediments on *P*-wave receiver functions, such as removing sedimentary response through wavefield downward continuation (Langston, 2011; Tao *et al.*, 2014), designing a resonance removal filter (Yu *et al.*, 2015) or using free-surface multiples for imaging (e.g., Chen *et al.*, 2006; Schmandt *et al.*, 2015), their applicability is still limited. *S*-wave receiver functions have the advantage of being free from *S*-wave multiples; however, the relative weak and low-frequency *S*-to-*P* conversion from the Moho can still be contaminated by noise of various origins, such as strong *P*-wave coda in sedimentary basins (e.g., Farra and Vinnik, 2000).

Recently, the virtual deep seismic sounding (VDSS) method was developed to image the Moho in regions with dense seismic arrays (Tseng *et al.*, 2009; Yu *et al.*, 2012, 2016). VDSS relies on the *SsPmp* phase—a wide-angle *PmP* reflection from the Moho, following the teleseismic *S*-wave incidence and an *S*-to-*P* conversion at the free surface (Zandt and Randall, 1985). The postcritical nature of the *SsPmp* phase makes it less sensitive to the detailed structure of the crust. Previous studies, including both synthetic waveforms and field observations, demonstrate the effectiveness of VDSS in the presence of either shallow sediments or a transitional crust–mantle boundary (Yu *et al.*, 2012; Kang *et al.*, 2016; Parker *et al.*, 2016; Liu *et al.*, 2018). To achieve the postcritical reflection from the Moho and to avoid waveform complexity due to a triplication, VDSS requires that the source–receiver distance is between about 30° and 50°. This constraint limits the application of VDSS to events having relatively large magnitudes, for example, $M_w > 5.5$.

In this study, we introduce a method that can determine the depth of the Moho using regional earthquakes. The method relies on *Pn* and its first crustal multiples *PnPn*. The difference between *PnPn* and *Pn* is essentially a critical *PmP* reflection from the bottom of the crust. The method is especially suitable for studying the Moho beneath sedimentary basins. Low-velocity sediments can significantly increase the *P*-to-*P* reflection coefficient near the surface. As a result, *PnPn* is strongly amplified, making it clearly visible even on a single record. In the following, we first introduce the methodology with synthetic examples. Then, we demonstrate its usefulness with data from two regional earthquakes. One of these occurred in the Imperial Valley near the United States–Mexico border, and the other occurred in Oklahoma in the central United States.

Methodology

Depending on the crustal thickness, *Pn* is the first arrival beyond distances of about 100–200 km for regional crustal earthquakes. For a flat-layered crustal model, its first crustal multiple, *PnPn*, arrives at a constant delay time after *Pn*. This is the case, regardless of the source–receiver distance. *PnPn* can travel along many different ray paths from the source to the receiver, but its energy mainly consists of *PmpPn* and *PnPmp* phases (one *Pn* leg merges to a *PmP* critical reflection near the source or the receiver; Fig. 1a,b). The delay time of *PnPn* with respect to *Pn* can be expressed as follows:

$$T_{PnPn-Pn} = 2H\sqrt{V_P^{-2} - p^2}, \tag{1}$$

in which V_P is the average crustal *P*-wavespeed, H is the crustal thickness, and p is the horizontal slowness of *Pn* (or the inverse of uppermost mantle *P*-wavespeed). At small epicentral distances, *PnPn* is masked by other strong crustal phases, such as direct *P*, *PmP*, and their depth phases. At larger regional distances, *PnPn* becomes well separated from other crustal phases (Fig. 1c,d). *PnPn* has been observed earlier in regional waveform modeling studies (e.g., Langston and Helmberger, 1974; Langston *et al.*, 2002), but it was not specifically used to study the Moho.

Verification with 1D Synthetics

For a continental crust without sedimentary basins, *PnPn* is small in amplitude (Fig. 1c). However, it is significantly amplified in the presence of shallow sediments (Fig. 1d). Low-velocity sediments cause the rays to steepen near the free surface; thus, they greatly increase the *P*-to-*P* reflection coefficient. Our 1D synthetic waveform modeling suggests that the amplitude of *PnPn* is even stronger than that of the *Pn* for a model with shallow sediments (2 km in thickness, 3 km/s in *P*-wavespeed; Fig. 1d). Because *PnPn* shares the same ray path as *Pn* near the source, its amplitude, arrival time, and wave shape, once normalized by the latter, are independent of earthquake source parameters such as focal mechanism and focal depth (Fig. 2). As a result, waveforms from nearby events or stations can be directly compared and/or stacked. Furthermore, the relative amplitude between *PnPn* and *Pn* is insensitive to the width of the crust–mantle transition (compared with Fig. 2a,b). Such properties of *PnPn* make it well suited for the study of the Moho beneath sedimentary basins, even if the Moho is a gradual boundary. We note that knowledge of earthquake source parameters and careful waveform analysis are still needed as other phases, such as depth phases, can potentially contaminate the *PnPn* phase (Fig. 2). Higher-order *Pn* multiples, such as *PnPnPn*, or *Sn* multiples (Chu and Helmberger, 2014) can also be used to study the Moho. For the purpose of this study, however, we will focus on *PnPn* only.

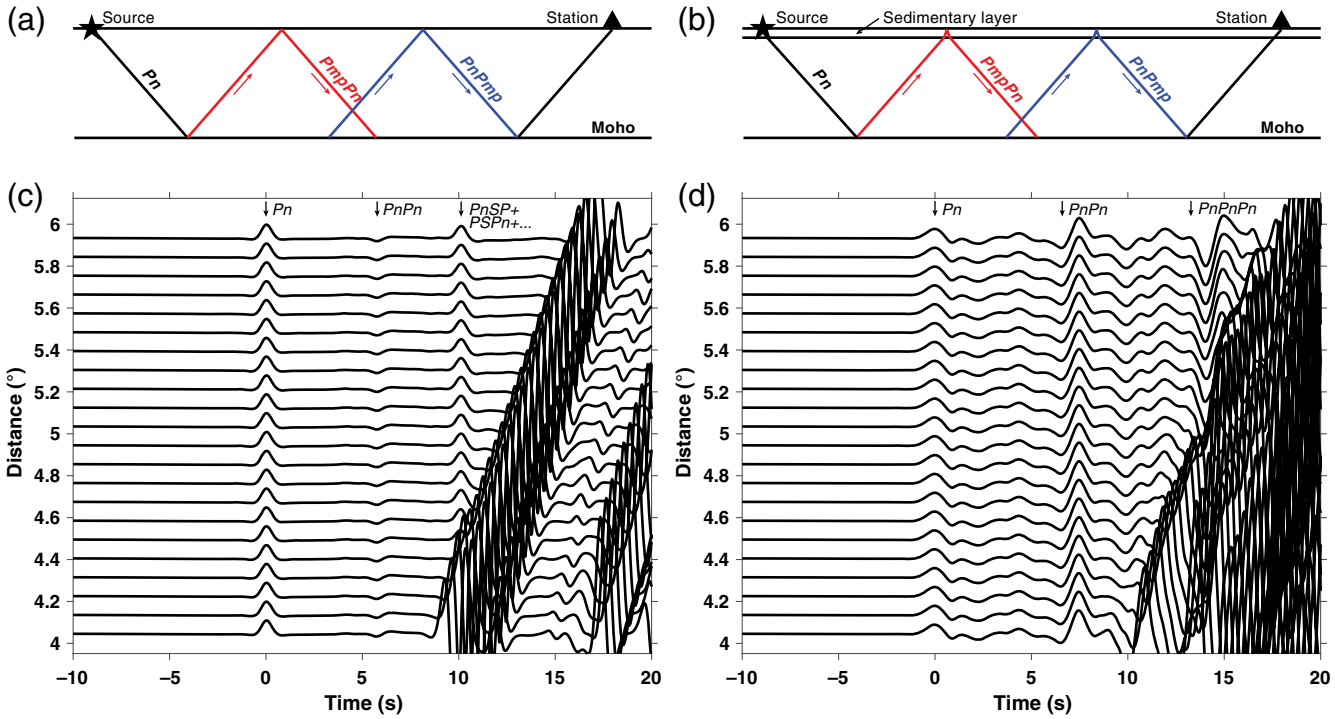

Figure 1. Schematic diagram showing ray paths of *Pn* and its crustal multiple *PnPn*, including *PmpPn* and *PnPmp*, for a 1D crust model (a) without and (b) with a sedimentary layer. The crust is 30 km thick, with a *P*-wavespeed of 6.3 km/s. The sediment is 2 km thick, with a constant *P*-wavespeed of 3 km/s. *S*-wavespeeds and densities are derived from the empirical relationship of Brocher (2005). (c,d) Vertical-component synthetic waveforms from model (a,b), respectively. Traces are normalized and aligned by the peak of *Pn*. A source at the free surface with a strike-slip focal mechanism is assumed. The arrival at around 10 s in (c) is a combination of multiples of *Pn* with three *P* legs and one *S* leg in the crust. The strong arrivals after about 8 s with slower propagation velocity are the direct *P* and *PmP*. The color version of this figure is available only in the electronic edition.

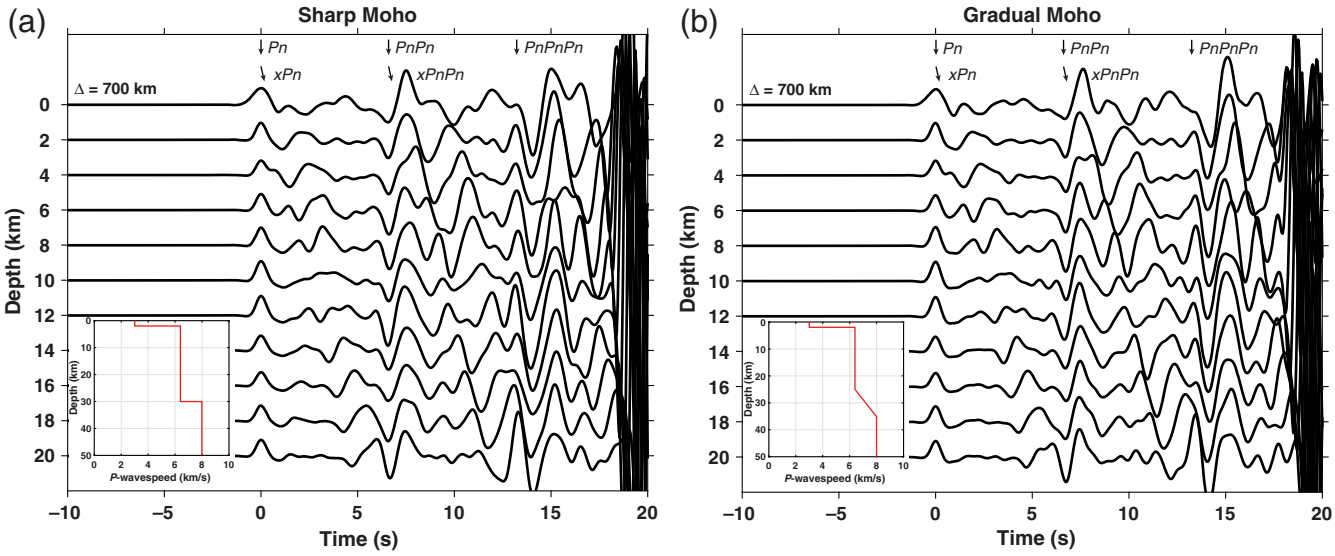

Figure 2. Synthetic *Pn* waveforms as a function of earthquake depth for (a) a sharp Moho and (b) a 10 km thick gradual Moho. The insets in each panel show the velocity model. Source focal mechanisms are the same as those used to calculate Figure 1c,d. The source–receiver distance is 700 km. The strong arrivals at about 18 s are the direct *P* and *PmP*. *xPn* represents the depth phases of *Pn*, which first travel upward to the free surface as a *P* or *S* wave and then reflect and propagate as *Pn* to the station (here, *pPn* is stronger than *sPn*). *xPnPn* represents the depth phases of *PnPn*. The color version of this figure is available only in the electronic edition.

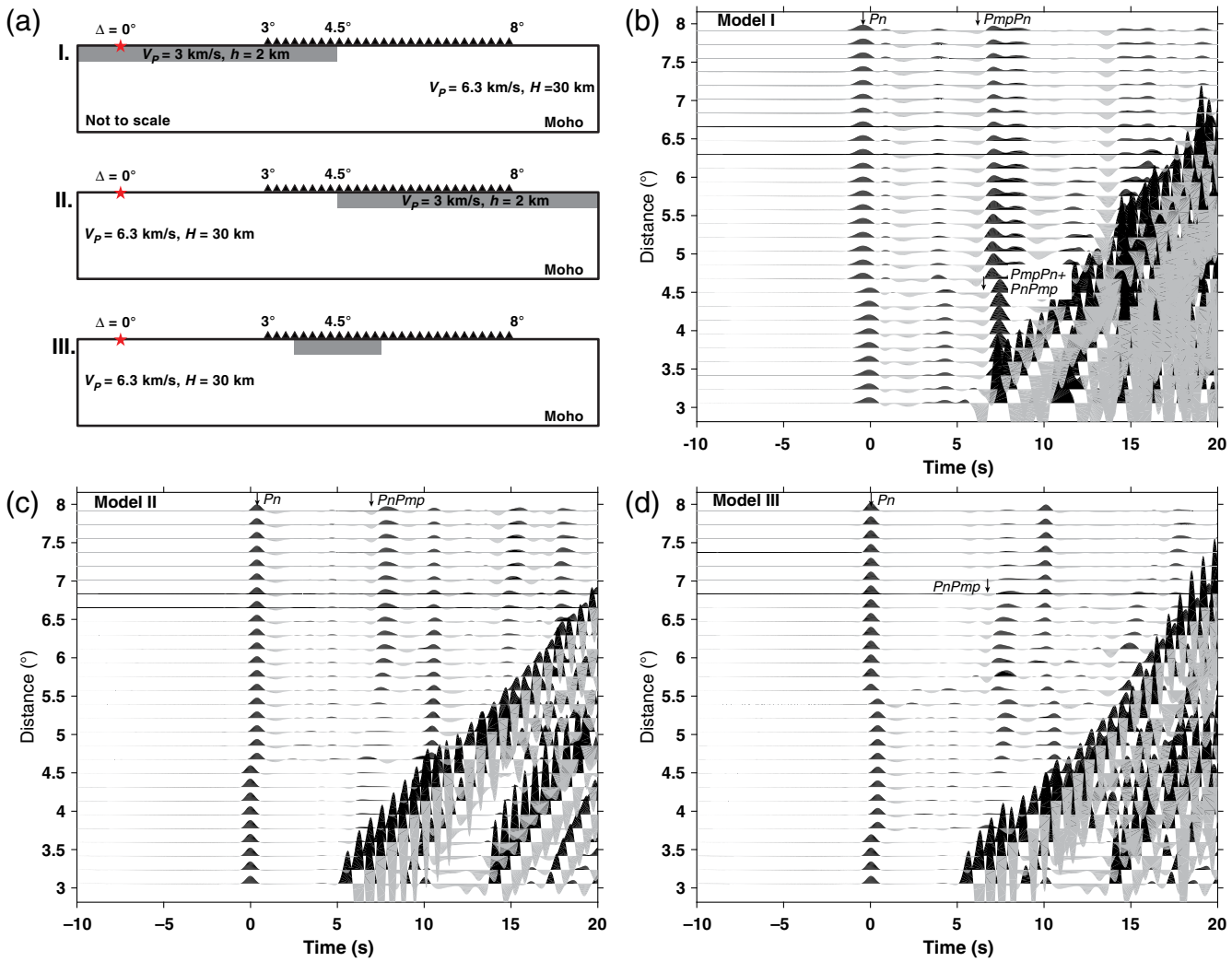

Figure 3. 2D synthetic waveform modeling with lateral variations in near-surface structure. (a) Three models (I, II, III) with different basin locations. Panels (b), (c), and (d) are synthetic waveforms generated from models I, II, and III, respectively. A reduction velocity of 8 km/s (same as uppermost mantle *P*-wavespeed) and a constant time shift are used to align waveforms (peak of *Pn* at zero time for stations at ~3°). The color version of this figure is available only in the electronic edition.

Sensitivity to 2D Shallow Structures

We further investigate the effect of lateral variations in near-surface structure on *PnPn*. Synthetic waveforms are computed using the GPU-based 2D finite-difference simulation method of Li *et al.* (2014). We consider three simple models (I, II, III) with sedimentary basins near the source, near the receiver, and in between, respectively (Fig. 3a). We use relatively large basins in I and II, mainly to make the effects more apparent and to minimize interference from other crustal phases. The sedimentary basins are 2 km deep, with a constant *P*-wavespeed of 3 km/s. The crust is 30 km thick, with a *P*-wavespeed of 6.3 km/s. Upper mantle *P*-wavespeed is 8 km/s. *S*-wavespeeds and densities are derived from the empirical relationship of Brocher (2005). For simplicity, because earthquake source parameters do not affect the relative behavior of *Pn* and its multiples, we assume a strike-slip earthquake focal mechanism with a hypocenter at the free surface.

Our synthetic waveforms demonstrate that *PmpPn* and *PnPmp* behave differently in the presence of lateral variation in the near-surface structure. In model I, the sedimentary basin is located near the source. For nearby (< 4.5°) stations, *PmpPn* and *PnPmp* contribute equally and their summed amplitude is large, similar to those in Figure 1d. For stations at greater distances, however, the major contribution to the amplitude comes from *PmpPn*. *PnPmp* is weak because the free-surface *P*-to-*P* reflection is outside the sedimentary basin. In contrast, in model II, *PmpPn* is not well-developed because there is no sediment near the source, but *PnPmp* is strong at large distance in which stations are located in the sedimentary basin. In model III, *PnPmp* is strong only when its free-surface *P*-to-*P* reflection point is in the sedimentary basin. The synthetic models suggest that *PnPn* (including *PmpPn* and *PnPmp*) is most sensitive to the Moho depth beneath the sedimentary basin, whether it is present near the source or the receiver.

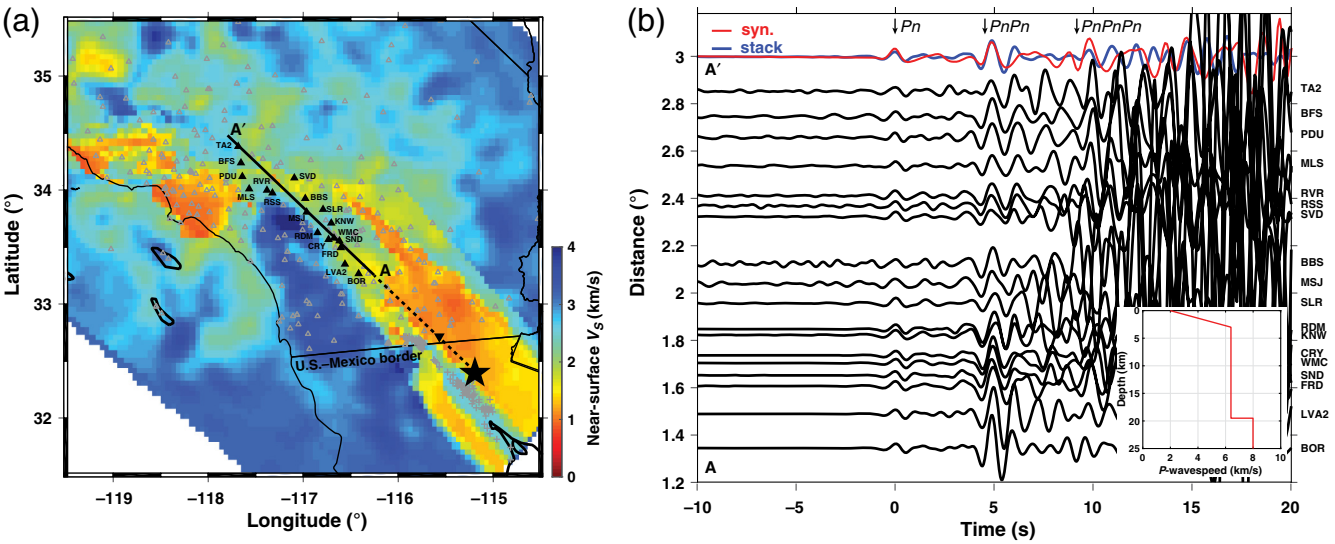

Figure 4. Observations and modeling of *PnPn* from an M_w 4.3 event in the Imperial Valley, California. (a) Map showing mean shear-wavespeed in the top 2 km from the Southern California Earthquake Center (SCEC) community velocity model CVM-S4.26 (Lee *et al.*, 2014). The event used in the study (black star) is an aftershock in the 2010 El Mayor–Cucapah earthquake sequence (gray pluses). Gray open triangles show the distribution of the Southern California Seismic Network (SCSN). Stations selected along a northwest–southeast profile (AA′), as indicated by the black solid triangles. (b) Seismic waveforms along profile AA′, normalized and manually aligned by *Pn*. A zero-phase, Butterworth band-pass filter between 0.5 and 1.5 Hz is applied. The stacked waveform (blue trace) and its synthetic fit (red trace) are shown at the top. (Inset) The best-fitting *P*-wave velocity model derived from waveform modeling. The color version of this figure is available only in the electronic edition.

Application to the Imperial Valley and Oklahoma

We validate our method using seismic data from two moderate-sized regional earthquakes in the Imperial Valley near the United States–Mexico border and in Oklahoma in the central United States.

Imperial Valley Event

The Imperial Valley in northern Baja California and southern California is covered by thick sediments. Recent high-resolution active-source studies near the Salton Sea suggest that the sedimentary layer extends to about 7 km depth near the center of the Imperial Valley (Han, Hole, Stock, Fuis, Williams, *et al.*, 2016; Persaud *et al.*, 2016). The sediment gradually shoals toward both the northeastern and southwestern edges of the valley. *P*-wavespeed increases continuously from ~2 km/s at the surface to ~6 km/s in the crystalline basement (Han, Hole, Stock, Fuis, Williams, *et al.*, 2016; Persaud *et al.*, 2016).

We examine an M_w 4.3 regional earthquake that was recorded along a northwest–southeast-trending profile, roughly parallel to the strike of the Imperial Valley, as shown in Figure 4a. The earthquake is an aftershock of the 2010 M_w 7.2 El Mayor–Cucapah earthquake and is located near the western flank of the Imperial Valley (Fig. 4a). The Southern California Seismic Network (SCSN) receivers that we use are located northwest of the earthquake (Fig. 4a). A zero-phase, Butterworth band-pass filter between 0.5 and 1.5 Hz is applied to the data. Figure 4b displays vertical-component *Pn* waveforms from the event. We identify *PnPn*, including *PmpPn* and *PnPmp*, as a strong, coherent phase that arrives at about 4–5 s after *Pn* with the same slowness but much larger amplitude (Fig. 4b). The seismicity in this region is limited to a depth that is less than about 10 km (Yu *et al.*, unpublished manuscript; see Data and Resources), so this strong phase cannot be a *Pn* depth phase. At epicentral distances less than about 1.9°, both *PmpPn* and *PnPmp* have their *P*-to-*P* reflection point in the sedimentary basin of the Imperial Valley. They merge to PmP^2 at a critical distance of about 1°. At epicentral distance larger than 1.9°, *PnPmp* plays a less important role than *PmpPn* because the sediment is much thinner near the receivers (Fig. 4a). As such, the observed *PnPn* is most sensitive to the crustal structure in the southwestern part of the Imperial Valley.

We perform 1D synthetic waveform modeling to estimate crustal thickness where the free-surface *P*-to-*P* reflection of the *PmpPn* phase occurs (inverted triangle in Fig. 4a). We assume a sedimentary thickness of 3 km with a linearly increasing *P*-wavespeed from 2 km/s at the free surface to 6.4 km/s at the basement (Persaud *et al.*, 2016). Below the sedimentary layer, the *P*-wavespeed is constant at 6.4 km/s in the crust and 8 km/s in the mantle. We search over crustal thicknesses from 15 to 30 km. The best-fitting crustal thickness determined by visual comparison is 19.5 ± 1.5 km (assuming a 3% uncertainty of crustal *P*-wavespeed; Fig. 4b), consistent with thin crust (~20 km) beneath the Imperial Valley, imaged with recent wide-angle seismic reflection and refraction profiles (Han, Hole, Stock, Fuis, Kell, *et al.*, 2016) or other datasets (Tape *et al.*, 2012).

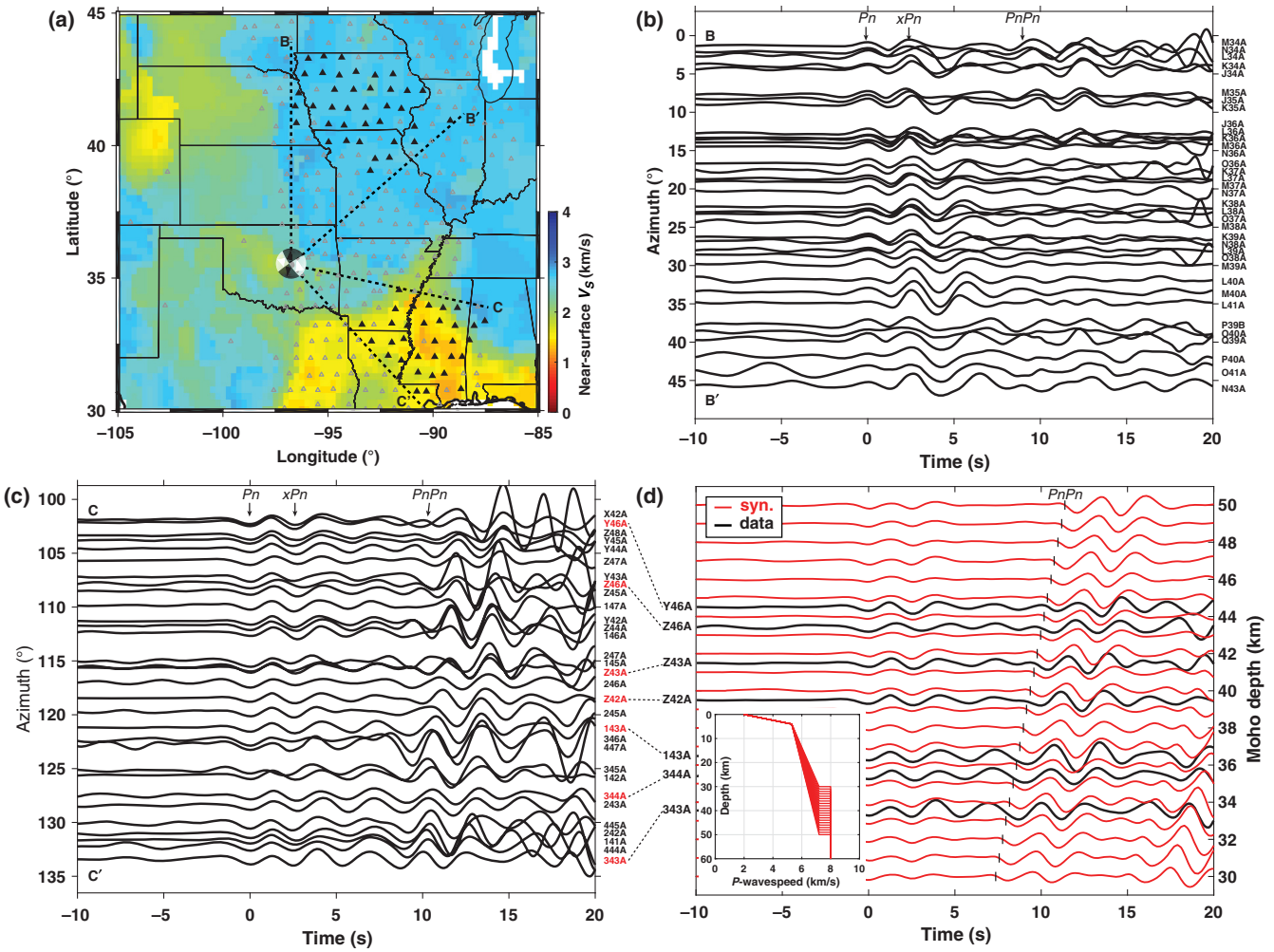

Figure 5. Observations and modeling of *PnPn* from the 2011 M_w 5.7 Oklahoma earthquake. (a) Map showing mean shear-wavespeed in the top 2 km from the model of Shen and Ritzwoller (2016). The event is well recorded by the USArray (triangles). The focal mechanism is from the U.S. Geological Survey National Earthquake Information Center. Panels (b) and (c) show azimuthal variations in *Pn* waveforms in the northeast and southeast clusters, respectively. Selected stations are marked as black solid triangles in (a). The source–receiver distance ranges in (b) and (c) are 4.6°–8.1° and 3.6°–8.3°, respectively. A zero-phase, Butterworth band-pass filter between 0.05 and 0.5 Hz is applied. *xPn* is the depth phase of *Pn*. (d) Comparison of synthetic *Pn* waveforms (red traces) with selected observations in the southeast cluster (black traces). Theoretical *PnPn* arrival times are indicated as short vertical bars. (Inset) *P*-wave velocity models used for synthetics. The best-fitting earthquake depth is 3 km. Note that the true earthquake depth may be slightly deeper because the near-surface velocity is higher in the source region. The color version of this figure is available only in the electronic edition.

2011 M_w 5.7 Prague, Oklahoma, Earthquake

Our second example uses data from the 2011 M_w 5.7 Prague earthquake in Oklahoma, recorded by USArray stations across the central United States. This earthquake was likely induced by wastewater injection as a result of disposal of wastewater, a byproduct of energy production (Keranen *et al.*, 2013). The event was well recorded by the USArray (Fig. 5a) and provides a rare opportunity to constrain lithospheric structures beneath the central United States (Chu and Helmberger, 2014).

We show two azimuthal profiles of seismic waveforms recorded to the northeast and southeast of the event (Fig. 5b, c). In both profiles, *Pn* and its depth phases (*xPn*; *x* represents *p* or *s*) are observed. The polarity of *Pn* is positive and negative for the northeast cluster and southeast cluster, respectively; this is consistent with the reported earthquake focal mechanism (U.S. Geological Survey National Earthquake Information Center; Fig. 5a). However, *PnPn* shows strong lateral variations in amplitude in the northeast cluster (Fig. 5b) and in arrival time in the southeast cluster (Fig. 5c). We interpret the former as a result of differences in the near-surface velocity structure near receivers and the latter as a result of differences in crustal thickness. Amplitudes of *PnPn* are large in the southeast cluster, in which most stations are underlain by thick, unconsolidated sediments in the Mississippi embayment (Fig. 5a).

We proceed to estimate crustal thickness for the southeast cluster, using a similar procedure as in the first example. The crustal velocity model is simplified from Shen and

Ritzwoller (2016), in which the sediment is 4 km in thickness with a linear increase of *P*-wavespeed from 2 km/s at the free surface to 5.3 km/s at the basement. Below the sedimentary layer, *P*-wavespeed increases linearly from 5.3 to 7.2 km/s. We search over crustal thicknesses from 30 to 50 km. By means of visual comparison of the synthetic waveforms with observations, we find that crustal thickness decreases southwestward from ~45 to ~33 km near the Mississippi embayment (Fig. 5d). The result is consistent with that determined from joint inversion of surface wave and receiver functions (Schmandt *et al.*, 2015; Shen and Ritzwoller, 2016). For the northeast cluster, *PnPn* is most clear within the azimuth range of 0°–15° (Fig. 5b). The estimated crustal thickness is ~40 km. Assuming a 3% perturbation of crustal *P*-wavespeed, uncertainties of above crustal thickness are ~8% of their absolute values.

Discussion

The method developed in this study can be considered as a vertically flipped analog of the conventional wide-angle seismic reflection method, in that both the source and the receiver are placed on the Moho and the reflection point at the free surface (Fig. 1a,b). Shallow sediments greatly increase the *P*-to-*P* reflection coefficient (in absolute sense) near the free surface, making it comparable to the critical *PmP* reflection coefficient (~1) from the Moho. On the other hand, *PnPn* undergoes a phase shift, which depends on the structure of the sedimentary layer. Although this study focuses on sedimentary effect on *Pn* waveforms, the relative amplitude between *PnPn* and *Pn* also depends on some other factors. These include geometrical spreading, velocity gradients in the uppermost mantle, and lateral structural variations (e.g., Kennett, 2001; Langston *et al.*, 2002). In our synthetic waveform modeling, we show that for a sedimentary layer with constant wavespeeds, the phase shift of *PnPn* is 180° with respect to *Pn* (Figs. 1 and 2). However, the phase shift is about 90° if the wavespeed increases linearly in the sedimentary layer (Fig. 5d). If the velocity structure of the sedimentary layer is unknown, the phase shift of *PnPn* can result in an additional uncertainty of about 1 km in Moho depth, assuming a phase uncertainty of 90° and a central frequency of 1 Hz.

The method is also similar to the VDSS method, which relies on the postcritical reflection, *SsPmp*, following the teleseismic *S*-wave incidence. Both methods measure the two-way vertical travel time in the crust via equation (1). In areas of gradual crust–mantle transition, both methods work well because the amplitudes of *PnPn* and *SsPmp* are insensitive to the width of the crust–mantle transition over the frequencies of interest (Fig. 2; Yu *et al.*, 2013).

There is an inherent trade-off between crustal thickness and crustal *P*-wavespeed in our method and all other reflection-based methods. For a constant delay time of *PnPn* with respect to *Pn*, estimated crustal thickness is anticorrelated with average crustal *P*-wavespeed (equation 1). For example, if the sedimentary layer in the Mississippi embayment is locally thicker or thinner than that used in the waveform simulation (Fig. 5d), we will likely overestimate or underestimate the crustal thickness. The observed azimuthal variation in *PnPn* arrival time, however, cannot be explained by the sedimentary effect because sedimentary thickness generally increases southwestward in the CC′ profile, not vice versa (Shen and Ritzwoller, 2016). On the other hand, the trade-off between crustal thickness and crustal *P*-wavespeed can be useful for tighter constraints of crustal buoyancy (Yu *et al.*, 2016).

The fact that our method works well for regions covered by thick sediments is both a strength and a weakness. On one hand, it can overcome difficulties in conventional seismic imaging methods (e.g., receiver functions), in which Moho signals are often strongly contaminated by sedimentary reverberations. On the other hand, our method is generally too weak to detect the Moho for regions that have no or very thin sedimentary basins (Figs. 1c and 5b). In addition, it may not work well if the sedimentary basin is very limited in horizontal extent. Nevertheless, we expect that our method can be widely applied to determine the depth of the Moho beneath large thick sedimentary basins, in the presence of moderate-sized seismicity and regional seismic recordings. It can complement other seismic methods in terms of providing a better understanding of both the global configuration and local features of the Moho.

Conclusions

We introduce a method to determine the depth of the Moho, utilizing the *Pn* crustal multiple *PnPn*. The differential travel time between *PnPn* and *Pn* is most sensitive to the crustal thickness as well as the average crustal *P*-wavespeed. A great advantage of the method is that it works especially well for regions covered by thick sediments, in which using conventional methods can be challenging. Low-velocity sediments can significantly amplify *PnPn*, making it clearly visible even on a single-seismic record. We verify the method with a series of 1D and 2D synthetic modeling, and we further validate it with two field examples; these took place in the Imperial Valley near the United States–Mexico border and in Oklahoma in the central United States. We suggest that the method can be applied to other regions covered by sedimentary basins.

Data and Resources

Broadband waveforms of southern California seismic stations were retrieved from the Southern California Seismic Network (SCSN), and USArray stations were retrieved from the Incorporated Research Institutions for Seismology (IRIS) Data Management Center (https://ds.iris.edu/ds/nodes/dmc/, last accessed March 2019). The focal mechanism of the 2011 M_w 5.7 Oklahoma earthquake is from the U.S. Geological Survey National Earthquake Information Center (https://

earthquake.usgs.gov/, last accessed March 2019). Depth of the 2010 El Mayor–Cucapah earthquake sequence is determined in the unpublished manuscript: C. Yu, E. Hauksson, Z. Zhan, E. S. Cochran, and D. V. Helmberger, "Depth Determination of the 2010 El Mayor–Cucapah Earthquake Sequence (M4.0)," *J. Geophys. Res.* (in revision).

Acknowledgments

The authors thank Chuck Langston and an anonymous reviewer for constructive reviews. Comments from Tom Brocher and Fred Pollitz are appreciated. This research was supported by National Science Foundation (NSF) Grant Numbers 1722879 and 1829496; U.S. Geological Survey/National Earthquake Hazards Reduction Program (USGS/NEHRP) Grant Numbers G16AP00147 and G18AP00028; and by the Southern California Earthquake Center (SCEC) (Award Number 17044), which is funded by NSF Cooperative Agreement EAR-1033462 and USGS Cooperative Agreement G12AC20038. The authors used waveforms and parametric data from the Caltech/USGS Southern California Seismic Network (SCSN), doi: http://dx.doi.org/10.7914/SN/CI; stored at the Southern California Earthquake Data Center, doi: http://dx.doi.org/10.7909/C3WD3xH1.

References

Anderson, D. L. (2007). *New Theory of the Earth*, Cambridge University Press, New York, New York.

Bath, M., and R. Stefánsson (1966). SP conversion at the base of the crust, *Ann. Geophys.* **19,** no. 2, 119–130.

Brocher, T. M. (2005). Empirical relations between elastic wavespeeds and density in the Earth's crust, *Bull. Seismol. Soc. Am.* **95,** no. 6, 2081–2092.

Brown, G. C., and A. E. Mussett (1993). *The Inaccessible Earth: An Integrated View to its Structure and Composition*, Second Ed., Chapman & Hall, London, United Kingdom.

Chen, L., T. Zheng, and W. Xu (2006). Receiver function migration image of the deep structure in the Bohai Bay Basin, eastern China, *Geophys. Res. Lett.* **33,** L20307, doi: 10.1029/2006GL027593.

Christensen, N., and W. Mooney (1995). Seismic velocity structure and composition of the continental crust: A global view, *J. Geophys. Res.* **100,** no. B6, 9761–9788.

Chu, R., and D. L. Helmberger (2014). Lithospheric waveguide beneath the Midwestern United States; massive low-velocity zone in the lower crust, *Geochem. Geophys. Geosyst.* **15,** no. 4, 1348–1362, doi: 10.1002/2013GC004914.

Eaton, D. W. (2006). Multi-genetic origin of the continental Moho: Insights from Lithoprobe, *Terra Nova* **18,** no. 1, 34–43.

Farra, V., and L. Vinnik (2000). Upper mantle stratification by P and S receiver functions, *Geophys. J. Int.* **141,** no. 3, 699–712.

Gilbert, H., A. A. Velasco, and G. Zandt (2007). Preservation of Proterozoic terrane boundaries within the Colorado Plateau and implications for its tectonic evolution, *Earth Planet. Sci. Lett.* **258,** nos. 1/2, 237–248, doi: 10.1016/j.epsl.2007.03.034.

Han, L., J. A. Hole, J. M. Stock, G. S. Fuis, A. Kell, N. W. Driscoll, G. M. Kent, A. J. Harding, M. J. Rymer, A. González-Fernández, *et al.* (2016). Continental rupture and the creation of new crust in the Salton Trough rift, Southern California and northern Mexico: Results from the Salton seismic imaging project, *J. Geophys. Res.* **121,** no. 10, 7469–7489, doi: 10.1002/2016JB013139.

Han, L., J. A. Hole, J. M. Stock, G. S. Fuis, C. F. Williams, J. R. Delph, K. K. Davenport, and A. J. Livers (2016). Seismic imaging of the metamorphism of young sediment into new crystalline crust in the actively rifting Imperial Valley, California, *Geochem. Geophys. Geosyst.* **17,** no. 11, 4566–4584, doi: 10.1002/2016GC006610.

Helmberger, D., and G. Engen (1980). Modeling the long-period body waves from shallow earthquakes at regional ranges, *Bull. Seismol. Soc. Am.* **70,** no. 5, 1699–1714.

Jordan, T. H., and L. N. Frazer (1975). Crustal and upper mantle structure from S_p phases, *J. Geophys. Res.* **80,** no. 11, 1504–1518.

Kang, D., C. Yu, J. Ning, and W. Chen (2016). Simultaneous determination of crustal thickness and P wavespeed by virtual deep seismic sounding (VDSS), *Seismol. Res. Lett.* **87,** no. 5, 1104–1111, doi: 10.1785/0220160056.

Kennett, B. L. (2001). *The Seismic Wavefield: Volume 2, Interpretation of Seismograms on Regional and Global Scales*, Cambridge University Press, New York, New York.

Keranen, K. M., H. M. Savage, G. A. Abers, and E. S. Cochran (2013). Potentially induced earthquakes in Oklahoma, USA: Links between wastewater injection and the 2011 Mw 5.7 earthquake sequence, *Geology* **41,** no. 6, 699–702, doi: 10.1130/G34045.1.

Langston, C. A. (1979). Structure under Mount Rainier, Washington, inferred from teleseismic body waves, *J. Geophys. Res.* **84,** no. B9, 4749–4762.

Langston, C. A. (2011). Wave-field continuation and decomposition for passive seismic imaging under deep unconsolidated sediments, *Bull. Seismol. Soc. Am.* **101,** no. 5, 2176–2190.

Langston, C. A., and D. V. Helmberger (1974). Interpretation of body and Rayleigh waves from NTS to Tucson, *Bull. Seismol. Soc. Am.* **64,** no. 6, 1919–1929.

Langston, C. A., A. A. Nyblade, and T. J. Owens (2002). Regional wave propagation in Tanzania, east Africa, *J. Geophys. Res.* **107,** no. B1, doi: 10.1029/2001JB000167.

Lee, E., P. Chen, T. H. Jordan, P. B. Maechling, M. A. Denolle, and G. C. Beroza (2014). Full-3-D tomography for crustal structure in southern California based on the scattering-integral and the adjoint-wavefield methods, *J. Geophys. Res.* **119,** no. 8, 6421–6451, doi: 10.1002/2014JB011346.

Li, D., D. Helmberger, R. W. Clayton, and D. Sun (2014). Global synthetic seismograms using a 2-D finite-difference method, *Geophys. J. Int.* **197,** no. 2, 1166–1183.

Liu, T., S. L. Klemperer, C. Yu, and J. Ning (2018). Post-critical SsPmp and its applications to virtual deep seismic sounding (VDSS)—1: Sensitivity to lithospheric 1-D and 2-D structure, *Geophys. J. Int.* **215,** no. 2, 880–894.

Mooney, W. D., and T. M. Brocher (1987). Coincident seismic reflection/refraction studies of the continental lithosphere: A global review, *Rev. Geophys.* **25,** no. 4, 723–742.

Nyblade, A. A., K. S. Vogfjord, and C. A. Langston (1996). P wave velocity of Proterozoic upper mantle beneath central and southern Asia, *J. Geophys. Res.* **101,** no. B5, 11,159–11,171.

O'Reilly, S. Y., and W. Griffin (2013). Moho vs crust-mantle boundary: Evolution of an idea, *Tectonophysics* **609,** 535–546.

Parker, E. H., Jr, R. B. Hawman, K. M. Fischer, and L. S. Wagner (2016). Estimating crustal thickness using SsPmp in regions covered by low-velocity sediments: Imaging the Moho beneath the Southeastern Suture of the Appalachian Margin Experiment (SESAME) array, SE Atlantic Coastal Plain, *Geophys. Res. Lett.* **43,** no. 18, 9627–9635.

Persaud, P., Y. Ma, J. M. Stock, J. A. Hole, G. S. Fuis, and L. Han (2016). Fault zone characteristics and basin complexity in the southern Salton Trough, California, *Geology* **44,** no. 9, 747–750, doi: 10.1130/G38033.1.

Prodehl, C., and W. D. Mooney (2012). *Exploring the Earth's Crust: History and Results of Controlled-Source Seismology*, Geol. Soc. Am. Memoir, Vol. 208, The Geological Society of America, Boulder, Colorado.

Schmandt, B., F.-C. Lin, and K. E. Karlstrom (2015). Distinct crustal isostasy trends east and west of the Rocky Mountain Front, *Geophys. Res. Lett.* **42,** no. 23, 10,290–10,298, doi: 10.1002/2015GL066593.

Shen, W., and M. H. Ritzwoller (2016). Crustal and uppermost mantle structure beneath the United States, *J. Geophys. Res.* **121,** no. 6, 2016JB012887, doi: 10.1002/2016JB012887.

Tao, K., F. Niu, J. Ning, Y. J. Chen, S. Grand, H. Kawakatsu, S. Tanaka, M. Obayashi, and J. Ni (2014). Crustal structure beneath NE China imaged by NECESSArray receiver function data, *Earth Planet. Sci. Lett.* **398,** 48–57.

Tape, C., A. Plesch, J. H. Shaw, and H. Gilbert (2012). Estimating a continuous Moho surface for the California unified velocity model, *Seismol. Res. Lett.* **83,** no. 4, 728–735, doi: 10.1785/0220110118.

Thybo, H., I. Artemieva, and B. Kennett (2013). Moho: 100 years after Andrija Mohorovicic, *Tectonophysics* **609,** 1–8.

Tseng, T.-L., W.-P. Chen, and R. L. Nowack (2009). Northward thinning of Tibetan crust revealed by virtual seismic profiles, *Geophys. Res. Lett.* **36,** no. 24, L24304, doi: 10.1029/2009gl040457.

Vinnik, L. (1977). Detection of waves converted from P to SV in the mantle, *Phys. Earth Planet. In.***15,** no. 1, 39–45.

Watts, A. B. (2001). *Isostasy and Flexure of the Lithosphere*, Cambridge University Press, Cambridge, New York.

Yu, C., W.-P. Chen, and R. D. van der Hilst (2016). Constraints on residual topography and crustal properties in the western United States from virtual deep seismic sounding, *J. Geophys. Res.* **121,** doi: 10.1002/2016JB013046.

Yu, Y., J. Song, K. H. Liu, and S. S. Gao (2015). Determining crustal structure beneath seismic stations overlying a low-velocity sedimentary layer using receiver functions, *J. Geophys. Res.* **120,** no. 5, 3208–3218, doi: 10.1002/2014JB011610.

Yu, C.-Q., W.-P. Chen, J.-Y. Ning, K. Tao, T.-L. Tseng, X.-D. Fang, Y. John Chen, and R. D. van der Hilst (2012). Thick crust beneath the Ordos plateau: Implications for instability of the North China craton, *Earth Planet. Sci. Lett.* **357,** 366–375, doi: 10.1016/j.epsl.2012.09.027.

Yu, C.-Q., W.-P. Chen, and R. D. van der Hilst (2013). Removing source-side scattering for virtual deep seismic sounding (VDSS), *Geophys. J. Int.* **195,** no. 3, 1932–1941, doi: 10.1093/gji/ggt359.

Zandt, G., and G. E. Randall (1985). Observations of shear coupled P waves, *Geophys. Res. Lett.* **12,** no. 9, 565–568.

Chunquan Yu
Zhongwen Zhan
Egill Hauksson
Donald V. Helmberger
Seismological Laboratory
California Institute of Technology
1200 E. California Boulevard MC 252-21
Pasadena, California 91125 U.S.A.
yucq@sustech.edu.cn

Elizabeth S. Cochran
Earthquake Science Center
U.S. Geological Survey
525 South Wilson Street
Pasadena, California 91106 U.S.A.

Manuscript received 6 December 2018;
Published Online 7 May 2019